Chapter 7

Magnetic Resonance (MR)-transverse relaxivity in bi-magnetic ensemble of isotropic-anisotropic nanosystems due to collective magnetic property

7.1 INTRODUCTION

The consideration of proton nuclear magnetic resonance while considering the MR-relaxivity mechanism is a potential approach to achieve upgraded bio-medical images [1-4]. As discussed in earlier chapters, MR-relaxivity gives the idea of contrast quality by considering an enhanced longitudinal (r_1)/transverse (r_2) relaxation rate. r_2 or r_1 related to an ensemble of MNPs is a potential approach to get enhanced MR-contrast efficiency [5-7]. Moreover, MR-transverse relaxivity can be monitored by considering modulation in magnetization, size of MNPs, the respective radius, as well as inhomogeneity in a magnetic field, etc. [8-12]. Generally, Iron Oxide and Zinc Ferrite as SPM nanosystems are efficient candidates to get superior MR-transverse relaxivity [13-15]. This is because of the exclusive dynamic magnetic nature of SPM systems.

Moreover, with an increase in SPM MNPs concentrations in an ensemble, the dominance of interaction strength among constituent SPM nanosystems results in frustrated states, as cluster SG state, superferromagnetism state, because of frustrated as well as competing spins [16-17]. Moreover, competing state development can modify the collective nature, further modulating MR-relaxivity [18, 19]. The evolution of frustrated states can monitor anisotropy energy, that governs energy barriers [20]. As a result, modification in magnetic anisotropy, flipping of spins as well as collective nature can affect the proton relaxation rate

[28-20]. Such evolution will give a unique direction, to achieve MR-relaxation enhancement in the frustrated magnetic state of MNPs ensembles.

In this Chapter, a cluster SG state is considered to explore the MR-relaxivity study in which Zinc Ferrite nanorods are ensembled with isotropic MNPs, γ-Fe_2O_3@$ZnFe_2O_4$. The modification in energy barrier as well as magnetic anisotropy is achieved. The structural correlations are performed by considering SAXS and SANS. The collective magnetic responses are explored with the help of ac susceptibility analysis. MR-relaxivity enhancement is found in an applied field of 1.41 T following TD-NMR analysis. Further, MR-relaxivity is considered in an applied field of 3T. The dominance of the frustrated state with potential r_2/r_1 value with various applied fields is explored by considering water proton dephasing.

7.2 EXPERIMENTAL DETAILS

The synthesis of Zinc ferrite assemblies is same as Chapter 2 for HCEZF [21] with a reaction time of 21 h. For maghemite synthesis, a modified co-precipitation is considered [23] considering oleic acid for surfactant. For, hybrid system development, an appropriate Zinc Ferrite ensemble is considered in Chloroform and the isotropic Maghemite MNPs are dispersed in 4 ml of Chloroform, following sonication for 30 mins. The dispersed solutions are mechanical stirred for mixing. After sonication, the dispersed solution is kept in hot air oven at 80°C for evaporation of solvent, collected after evaporation and followed by washing using ethanol and DI water with drying for 12 h and final powder is taken for characterizations. For Time Domain (TD)-NMR analysis, Bruker TD-NMR instrument is considered to have 1.41 T field as well as 60 MHz frequency. The rest of the instrumental details are similar to previous chapters.

7.3 RESULTS AND DISCUSSIONS
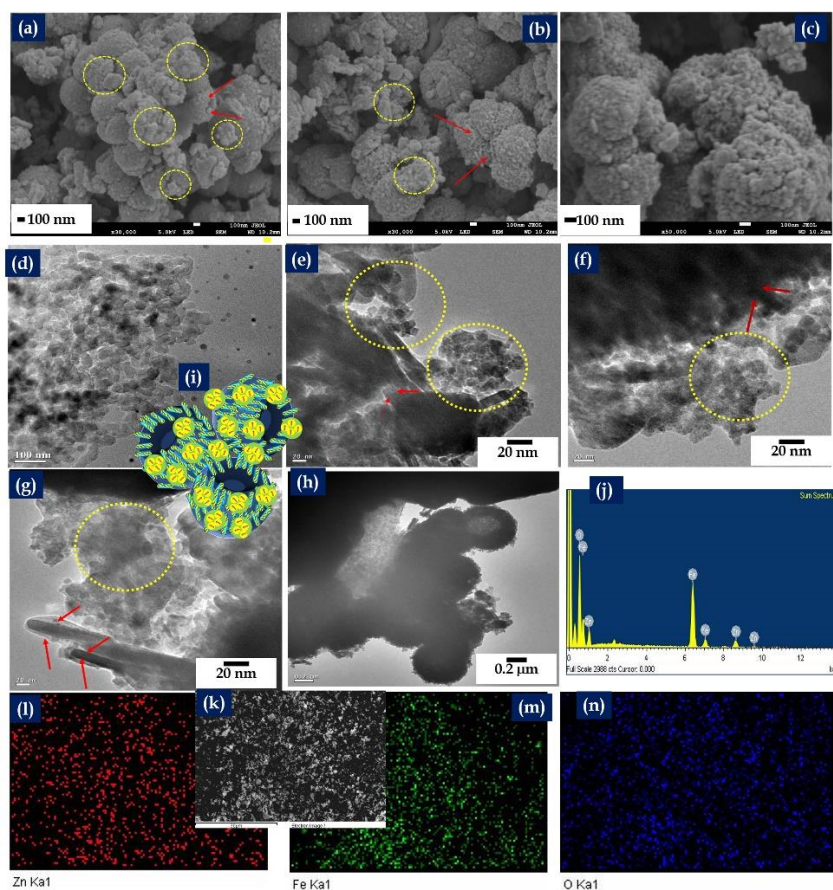
7.3.1 Microstructural study

Figure 7.1: FESEM micrographs at scale of (a, b, c) 100 nm, (d, e, f, g, h) TEM micrographs, (i) Schematic presentation of complex morphology; the EDX analysis: (j) Sum spectrum for present elements, (k) selected area EDX (30 µm), (l) for Zinc (Zn), (m) for Iron (Fe), and (n) for Oxygen (O) of γ-Fe$_2$O$_3$@ZnFe$_2$O$_4$. The big hollow ensemble is comprised of elongated shaped nanosystems, which represent the Zinc Ferrite ensemble and the small spherical shapes are used to represent the Iron-Oxide nanoparticles. However, the arrows are marked to illustrate blocked/freeze spins in a certain direction. In Figure (a), the yellow circle is provided to address the Iron Oxide nanoparticles and the red arrow is showing the broken ensemble.

FESEM analysis is executed to get morphological details as depicted in Figure 7.1(a-h). The Zinc Ferrite nanorods are arranged in their hierarchical pattern with an agglomeration of isotropic MNPs of maghemite as shown in the yellow mark depicted in Figure 7.1(a) and Figure 7.1(b). TEM images are depicted in Figure 7.1(d-h), which ensures the nanorods ensemble has an assembly of isotropic MNPs. For confirmation of expecting elements' presence, EDX analysis is performed as depicted in Figure 7.1(j-n) and respective atomic weights are given in Table 7.1. The intense peak for carbon is present in the low-energy region.

Table 7.1 Elementary composition details from EDX analysis.

Element	Weight %	Atomic %
Zn	11.99	5.05
Fe	46.08	22.7
O	41.94	72.2

To ensure the type of hierarchy, characterization of SAXS and SANS are performed as depicted in Figure 7.2(a). The intensity profile is represented to achieve both form factor and structure factor correlation. SAXS intensity profile is considered for fitting with three different contributions. In two contributions, structural information of primary MNPs is obtained and in one contribution, interparticle spacing information is achieved following log-normal distribution function [22], with r. In contribution 1, MNPs are fitted for a long cylinder form factor having 18 nm length (L), 2.6 nm radius (r) having 0.3 polydispersity index. This contribution is due to the scattering obtained from Zinc Ferrite nanorods of the ensembles.

Table 7.2: Fitted values of SAXS intensity profile.

| Contributions | Primary nanosystems from SAXS fitting | | | | | | |
| | Form Factor | | | | Structure Factor | | |
	Model	σ	r (nm)	L (nm)	Model	r (nm)	Fractal aggregation (nm)
1	Long cylinder	0.3	2.6	18	-	-	-
2	Sphere	0.5	2	-	Mass fractal	3.6	75
3	Sphere	0.4	2	-	-	-	-

The spherical form factor is taken having 2 nm MNPs with 0.5 polydispersity index, in contribution 2. The structure factor is also considered a mass fractal arrangement having r of 3.6 nm and a fractal aggregation 75 nm size. This scattering contribution is due to maghemite MNPs. However, for contribution 3, spherical model with log-norm distribution with a 2 nm size of 0.4 polydisperse index is considered. This contribution is a result of interparticle spacing among MNPs. Additionally, SANS profile fitting is executed with form factor of spherical model and achieved parameters are given in Table 7.2 and Table 7.3. The confirmation of two different assemblies is achieved from SANS fitting. The two-type of hierarchical arrangements of MNPs corroborate with the obtained parameters as represented in the Schematic in Figure 7.1(e).

Table 7.3: Fitted values of SANS intensity profile.

| Contribution | Secondary nanosystems from SANS fitting | | |
| | Form Factor | | |
	Model	σ	r (nm)
1	Sphere	0.03	398
2	Sphere	0.16	93

The XRD peaks are shown in Figure 7.2 (b) to ensure the crystalline phase and the respective planes of (220), (311), (222), (400), (422), (511), and (440) are found for γ-Fe_2O_3, and $ZnFe_2O_4$ with JCPDS numbers:39-1364 for γ-Fe_2O_3 and 82-1049 for $ZnFe_2O_4$. The plane (531) is due to γ-Fe_2O_3 and (533) is due to $ZnFe_2O_4$. Additionally, Raman analysis is executed for both pristine Zinc Ferrite and hybrid γ-Fe_2O_3@$ZnFe_2O_4$ as presented in Figure 7.2 (c). The respective Raman intensity peak at 325.0 cm^{-1} ensure $F_{2g}(2)$ mode, peak at 481.0 cm^{-1} is due to $F_{2g}(3)$ mode, and the most intense A_{1g} mode is found at 671.0 cm^{-1} due to Zinc Ferrite. The peak at 325.0 cm^{-1} is for $F_{2g}(2)$, 481.0 cm^{-1} for $F_{2g}(3)$, and 671.0 cm^{-1} for A_{1g} of $ZnFe_2O_4$. In γ-Fe_2O_3, respective mode at 289.0 cm^{-1} is for E_g, 481.0 cm^{-1} if for T_{2g}, and 671.0 cm^{-1} is for A_{1g}, with two additional modes at 1343 cm^{-1} and 1585 cm^{-1} confirming maghemite phase [23-25]. Figure 7.2(d-f) shows XPS analysis to achieve surface chemical compositions as shown in Figure 7.2 (d-f). The Zinc 2P spectrum is comprised of Zn $2p_{3/2}$ and Zn $2p_{1/2}$ peaks at 1021.3 eV as well as 1044.5 eV as given in the Figure 7.2 (d), having ΔE of 23.2 eV, confirming the purity of $ZnFe_2O_4$. Additionally, Fe^{3+} ions of $ZnFe_2O_4$ and γ-Fe_2O_3 are ensured by the intense peaks that are found at around 710.5 eV for Fe $2P_{3/2}$ and 724 eV for Fe

183

2P$_{1/2}$ as depicted in Figure 7.2 (e). The O 1s spectrum are depicted in Figure 7.2 (f). The peaks 529.8 eV along with 531.7 eV are related to lattice oxygens for both ZnFe$_2$O$_4$ and γ-Fe$_2$O$_3$ [23-25].
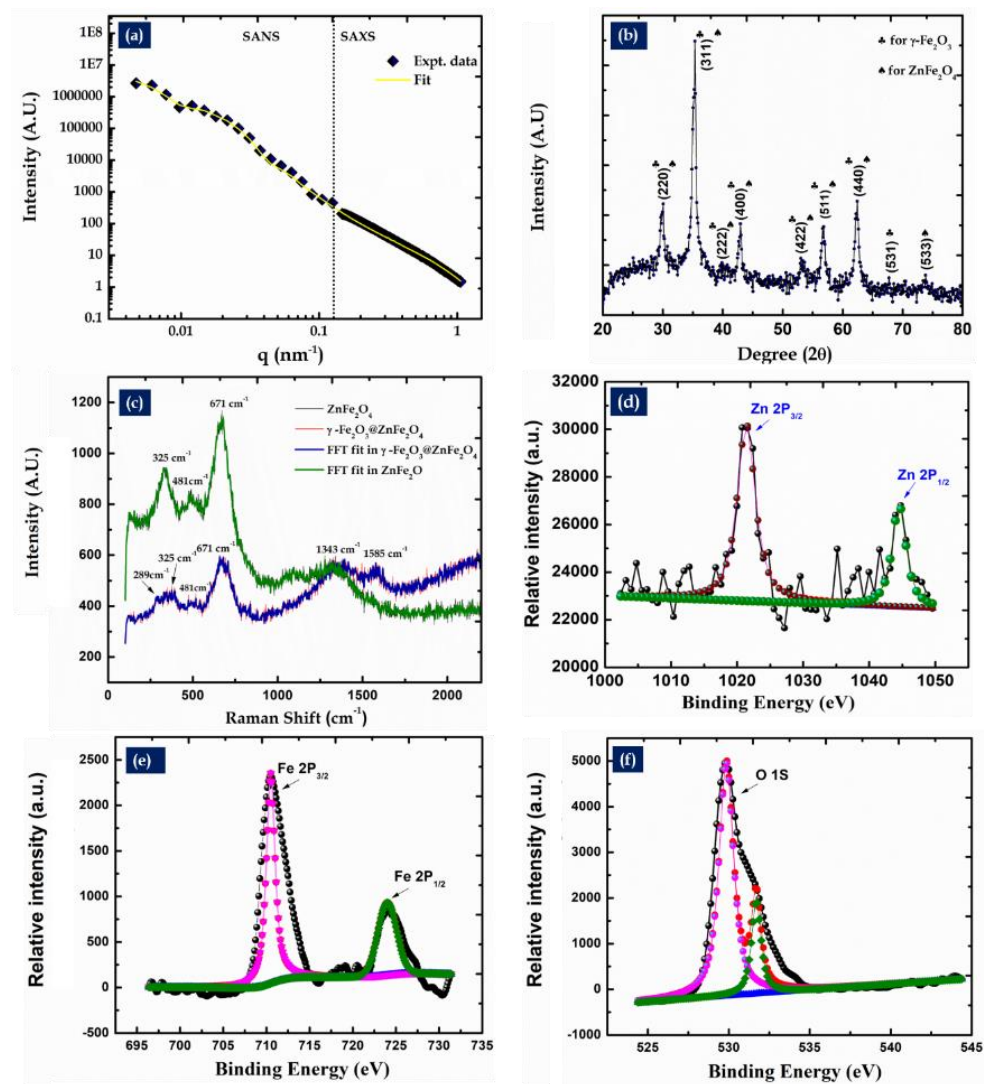

Figure 7.2: (a) SAXS and SANS fitting, (b) XRD pattern, (c) Raman plots; XPS study of (d) Zinc 2P, (e) Iron 2P, and (f) Oxygen 1S spectrum of γ-Fe$_2$O$_3$@ZnFe$_2$O$_4$.

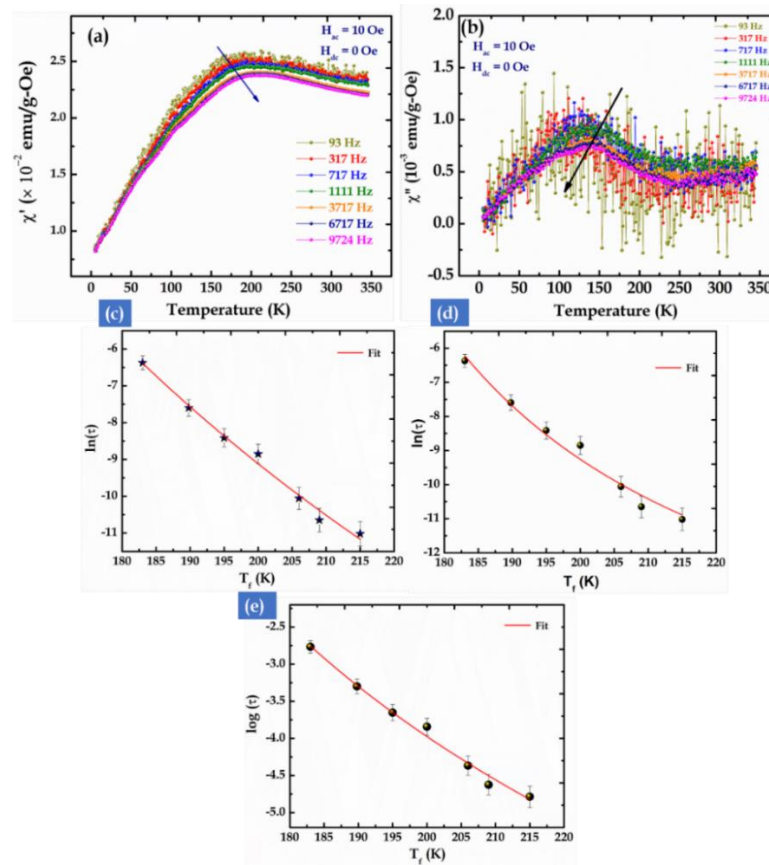**7.3.2 Dynamic magnetic study**

Figure 7.3: Real component ac susceptibility (a), imaginary component ac susceptibility (b); (c) Arrhenius law fitting, (d) VF law fitting, (e) Critical slowing down fitting of γ-Fe$_2$O$_3$@ZnFe$_2$O$_4$. The arrow mark indicates the change in T$_{max}$ and χ_{max} with an increase in frequency in Figure (a, b). The error bars are for standard deviation representation.

The analysis is executed with no DC field having an ac field of 10 Oe, for 2-350 K range with frequency ranges of 93 Hz to 9724 Hz as depicted in Figure 7.3(a, b). The in-phase ac susceptibility is given in Figure 7.3(a) and out-of-phase ac susceptibility is given in Figure 7.3(b). When the frequency is enhanced, the temperature maxima is observed to lower. Such nature is found in interacting SPM or SSG states. The non-zero imaginary ac susceptibility, χ'', is a signature of the SG state or interacting SPM state. A typical noise is observed at a low frequency range in χ''. The Mydosh parameter, k, is calculated with equation 2.9

185

of chapter 2. Herein, k gives as 0.08. This value lies in the range of interacting SPM state or in cluster SG systems [26-28].

The Arrhenius law fitting is employed for the frequency-dependent temperature peak following the equation 2.10 of Chapter 2. The achieved linear fitting as shown in Figure 7.3(c), gives activation energy, $\frac{E_a}{k_B}$ as 5880 K along with spin flipping, τ_0 of $\sim 1.9 \times 10^{-17}$ s. The values are unphysical and therefore the presence of a non-interacting SPM state is discarded. Further Vogel-Fulcher (VF) model is considered for fitting of transition temperature following equation 2.11 of Chapter 2. The proper fitting as depicted in Figure 7.3(d), gives flipping time, τ_0 of 1.2×10^{-8} s with activation energy, $\frac{E_a}{k_B} = 597.4$ K, and VF temperature of $T_0 = 133$ K. The energy barrier is achieved as 8.2×10^{-14} erg and non-zero VF temperature confirms the dominance of spin interaction. Moreover, τ_0 comes in cluster SG systems range. It is found that $\frac{E_a}{k_B} \sim 4.5$ T_0, confirms existence of interacting entities.

To confirm pure-SG state or interacting SPM state dominance in the system, a critical slowing model is taken, as mentioned in equation 2.13 of Chapter 2 and the fitting is depicted in Figure 7.3(e). After fitting, a critical exponent, zv' is achieved as 9.9, spin-flip time is achieved as $\tau^* = 1.8 \times 10^{-7}$ s and glass transition temperature, T_g is found as 131 K. The obtained values of critical exponent as well as spin relaxation confirm the dominance of the cluster-SG state. The highly interacting MNPs result in complex anisotropy, that triggers a frustrated magnetic state. Consideration of such a frustrated state is a novel approach to get enhanced MR-relaxivity.

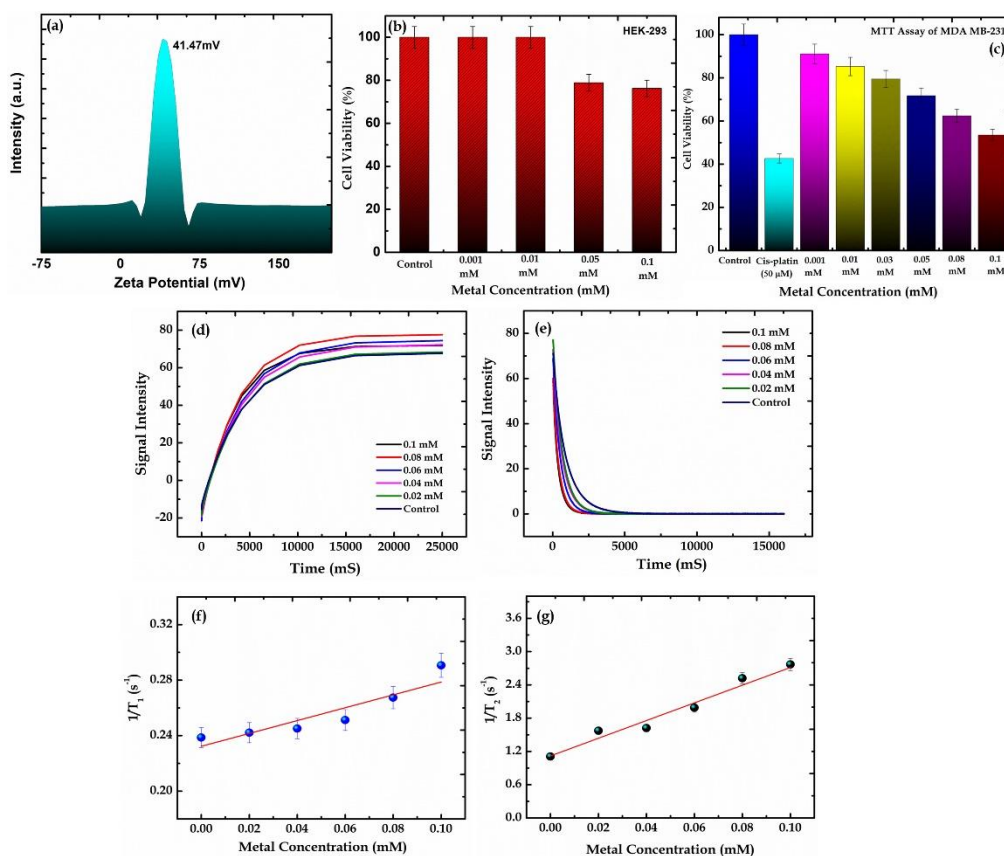## 7.3.3 Zeta potential and MTT assay

Figure 7.4: (a) Zeta potential plot, (b) MTT-assay in HEK-293 cell, (c) MTT-assay in MDA-MB-231 cancer cell; Intensity in signal for both longitudinal relaxation (d), for transverse relaxation (e) at various metal concentrations; (f) $1/T_1$ vs. Metal concentration curve to attain r_1; (g) $1/T_2$ vs. Metal concentration to get r_2 of γ-$Fe_2O_3@ZnFe_2O_4$. The error bars are for standard deviation representation.

In Figure 7.4(a), Zeta potential analysis is executed to get the idea of steric stability in the dispersion state. The Zeta potential, ξ, at neutral pH is found as 41.47 mV, confirming long-term emulsion stability in the agarose solution [19]. Moreover, an *in vitro* cytotoxic study is performed in HEK-293 cell line as depicted in Figure 7.4 (b). The hybrid system ensures cell viability. Additionally, cell viability is also executed in the breast cancer cell line with the aid of MDA-

MB 231 cell-line as depicted in Figure 7.4 (c). The system is showing dose-dependent cytotoxicity to MDA-MB 231 having 91% cell-viability at concentration of 0.001 mM, 85.3% at 0.01mM, 79.4% at concentration of 0.03 mM, 71% for 0.05 mM concentration, 62% for 0.08 mM, and 53% viability at concentration of 0.1 mM. The proton NMR relaxation is executed by considering the time-domain NMR study as provided in the next section.
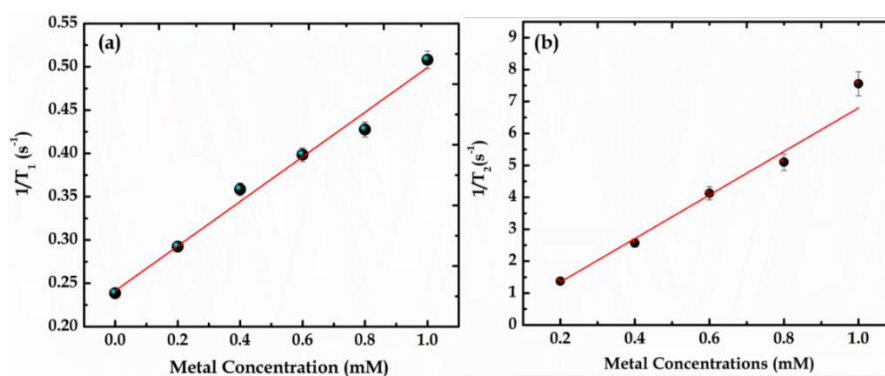
7.3.4 Time Domain NMR:

Figure 7.5 Pristine $ZnFe_2O_4$: (a) $1/T_1$ vs. Metal concentration curve to attain the longitudinal relaxivity (r_1) and (b) $1/T_2$ vs. Metal concentration to attain the transverse relaxivity (r_2). The error bars in the data represent standard deviation in experimental data.

TD-NMR analysis is executed with five various metal concentrations including 0.02, 0.04, 0.06, 0.08, and 0.1 mM respectively in 1.41 T field as depicted in Figure 7.4(d-g). The systems are stabilized in agarose solution to perform the relaxivity study at 300 K [19]. The signal intensity obtained from TD-NMR is displayed in Figure 7.4(d) in case of longitudinal relaxation as well as Figure 7.4(e) for transverse relaxation. The trend of $1/T_1$ and $1/T_2$ with metal concentration is depicted in Figure 7.4(f) and Figure 7.4(g). The value for r_1 is found as 0.46 s^{-1}mM^{-1} and r_2 is found to be 15.94 s^{-1}mM^{-1}, with r_2/r_1 of 34.65. As the calculated value is greater than 10, which ensures MR-transverse relaxivity dominance. The

relaxivity of bare Zinc Ferrite ensemble is also executed and the signal intensities are given in Figure 7.5. r_1 and r_2 for $ZnFe_2O_4$ is found as 0.25 s^{-1}mM^{-1} and 6.81 s^{-1}mM^{-1} at 1.41 T, with r_2/r_1 of 27.2. It is found that the hybrid system gives enhanced efficacy of MR-transverse relaxivity, with potential applicability in MR imaging [29].
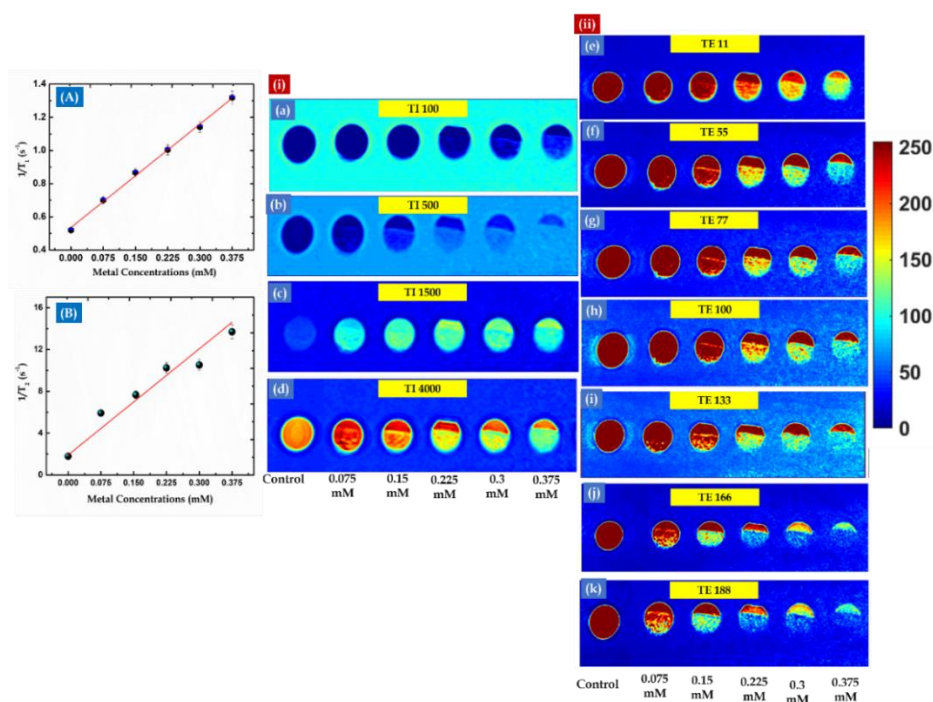

Figure 7.6: (A) Longitudinal relaxivity plot, (B) Transverse relaxivity plot, Phantom images in case of (i) Longitudinal relaxation with TI, and (ii) Transverse relaxation with various TE of γ-Fe$_2$O$_3$@ZnFe$_2$O$_4$.

MRI- *in vitro* phantom micrographs are given in Figure 7.6 having TI along with TE with a slightly more metal concentration to check MR-signal efficiency. The phantom images of longitudinal relaxivity are achieved with a range of TI, such as 100 ms, 500 ms, 1500 ms, and 4000 ms as depicted in Figure 7.6(i); and transverse relaxivity-based phantom signals with TE for a range of 11ms, 55ms, 77ms, 100ms, 133ms, 166ms, and 188 ms, as depicted in Figure 7.6(ii). The phantom signals are observed at 3 T field. The enhancement in signal intensity is

seen with increase in metal concentration. MR-relaxivity trend is examined with a series of metal concentrations at 3 T as depicted in Figure 7.6(A) and Figure 7.6(B). The signal intensity fitting with various TI having a series of metal concentrations is performed following equation 5.8 of chapter 5. The TI is considered as 100-4000 ms and 5000 ms TR and 12 ms TE. The non-linear fitting gives T_1 for all the considered metal concentrations. To achieve r_1, corresponding fitting of T_1 for all the metal concentrations are shown in Figure 7.6(A) with equation 5.9 of Chapter 5.

With metal concentration variation, T_2 is achieved with proper fitting of transverse signal intensity (M_{TE}) with the help of equation 5.10 of Chapter 5. The respective fitting is observed in Figure 7.6 (B). After linear fitting of $1/T_2$ with respect to metal concentrations, with equation 5.9 of Chapter 5, r_2 is achieved and r_1 and r_2 at 3T are found as: 2 $s^{-1}mM^{-1}$ and 33.8 $s^{-1}mM^{-1}$. As a result, r_2/r_1 is achieved as 16.9. As $r_2/r_1 > 10$, further confirming the dominance of MR-transverse relaxivity [31-41]. The MR-relaxivity is highly sensitive towards magnetic field. The system ensures superior efficacy in transverse relaxivity at a low field with a minimal 0.1 mM metal concentration. The hybrid system with a frustrated magnetic state triggers slow spin dynamics, with competing spin domains that enhances anisotropy landscape complexity. The complexity involved in the structure as well as the magnetic frustrated state in the system triggers enhancement in MR-relaxivity. With enhanced anisotropy energy, local magnetic field inhomogeneity enhances and as a result, faster decay of transverse as well as longitudinal relaxation is observed. The enhancement in shape anisotropy after incorporating the maghemite MNPs shows superior r_2/r_1.

7.4 CONCLUDING REMARKS

In conclusion, a novel approach to attaining enhanced MR-relaxivity by considering a cell-viable cluster SG system is addressed, γ-Fe$_2$O$_3$@ZnFe$_2$O$_4$. The collected magnetic nature is evaluated with 1.20×10^{-8} s spin flipping time along with 8.2×10^{-14} erg energy barrier. The non-zero VF temperature with a 9.9 critical exponent, with a glass transition temperature of 131 K confirms the cluster SG state. The maghemite MNPs are following mass fractal arrangement and Zinc Ferrite nanorods are arranged hierarchically. The induced structural complexity leads to enhancement in magnetic anisotropy as well as field inhomogeneity. Such SG-glass spin dynamic is observed as triggering faster proton decay in MR-transverse relaxivity. The significant signal-enhancement is evident in *in vitro* MRI with superior r_2/r_1 with a 0.1 mM low concentration.

References:

[1] Usman, M. S., Hussein, M. Z., Fakurazi, S. and Saad, F. F. A. Gadolinium-based layered double hydroxide and graphene oxide nano-carriers for magnetic resonance imaging and drug delivery, *Chemistry Central Journal,* 11:1, 2017.

[2] Tagami, T., Foltz, W. D., Ernsting, M. J., Lee, C. M., Tannock, I. F., May, J. P. and Li, S. D. MRI monitoring of intratumoral drug delivery and prediction of the therapeutic effect with a multifunctional thermosensitive liposome**,** *Biomaterials,* 32:6570, 2011.

[3] Chertok, B., Moffat, B. A., David, A. E., Yu, F., Bergemann, C., Ross, B. D. and Yang, V. C. Iron oxide nanoparticles as a drug delivery vehicle for MRI monitored magnetic targeting of brain tumors. *Biomaterials,* 29:487, 2008.

[4] MacMahon, E. and Brougham, D. F. pH Dependence of MRI Contrast in Magnetic Nanoparticle Suspensions Demonstrates Inner-Sphere Relaxivity

Contributions and Reveals the Mechanism of Dissolution. *Langmuir*, 39:2171, 2023.

[5] Miao, Y., Zhang, H., Cai, J., Chen, Y., Ma, H., Zhang, S., Bao, J., Liu, X., Bay, B., Guo, Y., Gu, N. and Fan, H. Structure–Relaxivity Mechanism of an Ultrasmall Ferrite Nanoparticle T1 MR Contrast Agent: The Impact of Dopants Controlled Crystalline Core and Surface Disordered Shell. *Nano Letters,* 21:1115, 2021.

[6] R.A. Brooks, F. Moiny, and P. Gillis, On T_2-shortening by weakly magnetized particles: The chemical exchange model. *Magnetic Resonance Medicine*, 1020: 1014, 2001.

[7] Villaraza, A. J. L., Bumb, A. and Brechbiel, M. W. Macromolecules, Dendrimers, and Nanomaterials in Magnetic Resonance Imaging: The Interplay between Size, Function, and Pharmacokinetics. *Chemical Reviews*, 110:2921, 2010.

[8] Yang, L., Wang, Z., Ma, L., Li, A., Xin, J., Wei, R., Lin, H., Wang, R., Chen, Z. and Gao, J. The Roles of Morphology on the Relaxation Rates of Magnetic Nanoparticles. *ACS Nano*, 12:4605, 2018.

[9] Zhou, Z., Zhao, Z., Zhang, H., Wang, Z., Chen, X., Wang, R., Chen, Z. and Gao, J. Interplay between Longitudinal and Transverse Contrasts in Fe_3O_4 Nanoplates with (111) Exposed Surfaces. *ACS Nano*, 8:7976, 2014.

[10] Zhou, Z., Tian, R., Wang, Z., Yang, Z., Liu, Y., Liu, G., Wang, R., Gao, J., Song, J., Nie, L. and Chen, X. Artificial local magnetic field inhomogeneity enhances T_2 relaxivity. *Nature Communications,* 8:15468, 2017.

[11] Dormann, J. L., Fiorani, D., Cherkaoui, R., Tronc, E., Lucari, F., D'Orazio, F., Spinu, L., Noguès, M, Kachkachi, H. and Jolivet, J. P. From pure superparamagnetism to glass collective state in γ-Fe_2O_3 nanoparticle assemblies. *Journal of Magnetism and Magnetic Materials,* 203:23, 1999.

[12] Grinolds, M. S., Hong, S., Maletinsky, P., Luan, L., Lukin, M. D., Walsworth, R. L. and Yacoby, A. Nanoscale magnetic imaging of a single electron spin under ambient conditions. *Nature Physics*, 9:215, 2013.

[13] Rugar, D., Mamin, H. J., Sherwood, M. H., Kim, M., Rettner, C. T., Ohno, K. and Awschalom, D. D. Proton magnetic resonance imaging using a nitrogen–vacancy spin sensor. *Nature Nanotechnology.* 10:120., 2015.

[14] Zhou, Z., Bai, R., Munasinghe, J., Shen, Z., Nie, L. and Chen, X. T_1-T_2 Dual-Modal Magnetic Resonance Imaging: From Molecular Basis to Contrast Agents. *ACS Nano*, 11:5227, 2017.

[15] T. Simsek, and S. Özcan, S. Effective magnetic anisotropy enhancement of FePt nanocrystals through shape control. *Journal of Magnetism and Magnetic Materials*, 351:47, 2014.

[16] Kostevsek, N. A Review on the Optimal Design of Magnetic Nanoparticle-Based T2 MRI Contrast Agents. *Magnetochemistry*. 6:11, 2020.

[17] Reyes-Ortega, F., Delgado, A. V. and Iglesias, G. R. Modulation of the Magnetic Hyperthermia Response Using Different Superparamagnetic Iron Oxide Nanoparticle Morphologies. *Nanomaterials*, 11:627, 2021.

[18] Aflori, M. Smart Nanomaterials for Biomedical Applications—A Review. *Nanomaterials*, 11:396, 2021.

[19] Saikia, K., Bhattacharya, K., Sen, D., Kaushik, SD., Biswas, J., Lodha, S., Gogoi, B., Buragohain, AK., Kockenberger, W. and Deb, P. Solvent evaporation driven entrapment of magnetic nanoparticles in mesoporous frame for designing a highly efficient MRI contrast probe. *Applied Surface Science*, 464:567, 2019.

[20] Peeters, D., Taffa, D. H., Kerrigan, M. M., Ney, A., Jöns, N., Rogalla, D., Cwik, S., Becker, H.-W., Grafen, M., Ostendorf, A., Winter, C. H., Chakraborty, S., Wark,

M. and Devi, A. Photoactive Zinc Ferrites Fabricated via Conventional CVD Approach. *ACS Sustainable Chemistry & Engineering*, 5:2917, 2017.

[21] Zhou, X., Li, H., Sun, X., Sun, P., Liang, X., Liu, F., Hu, X. and Lu, G. Nanosheet-Assembled $ZnFe_2O_4$ Hollow Microspheres for High-Sensitive Acetone Sensor. *ACS Applied Materials Interfaces*, 7:15414, 2015.

[22] Kohlbrecher, J. SASfit: A program for fitting simple structural models to small angle scattering data, 2023.

[23] Saikia, K., Sarma, D. D. and Deb, P. Organization dependent collective magnetic properties of secondary nanostructures with differential spatial ordering and magnetic easy axis orientation. *Journal of Magnetism and Magnetic Materials*. 127:408, 2016.

[24] Guo, Y., Zhang, N., Wang, X., Qian, Q., Zhang, S., Li, Z. and Zou, Z. A facile spray pyrolysis method to prepare Ti-doped $ZnFe_2O_4$ for boosting photoelectrochemical water splitting. *Journal of Material Chemistry A,* 5:7571, 2017.

[26] Jain, S., Shah, J., Negi, N. S., Sharma, C. and Kotnala, R. K. Significance of interface barrier at electrode of hematite hydroelectric cell for generating ecopower by water splitting. *International Journal of Energy Research*, 43:4743, 2019.

[27] Bag, P., Baral, P. R. and Nath, R. Cluster spin-glass behavior and memory effect in $Cr_{0.5}Fe_{0.5}Ga$. *Physical Review B*, 98:144436, 2018.

[28] Stimpson, L. J. V., Powell, J. M., Stenning, G. B. G., Jura, M. and Arnold, D. C. Spin-glass behavior in $K_xRu_{4-y}Ni_yO_8$ hollandite materials. *Physical Review B*, 98:174429, 2018.

[29] Usov, N. A. and Serebryakova, O. Equilibrium properties of assembly of interacting superparamagnetic nanoparticles. *Scientific Reports*, 10:13677, 2020.

194

[30] Zhou, Z., Yang, L., Gao, J. and Chen, X. Structure–Relaxivity Relationships of Magnetic Nanoparticles for Magnetic Resonance Imaging. *Advanced Materials*, 31:1804567, 2019.

[31] A. Guleria, P. Pranjali, M. K. Meher, A. Chaturvedi, S. Chakraborti, R. Raj, K. Poluri, and D. Kumar, Effect of Polyol Chain Length on Proton Relaxivity of Gadolinium Oxide Nanoparticles for Enhanced Magnetic Resonance Imaging Contrast. *Journal of Physical Chemistry C*, 123:18061, 2019.

[32] B. Thapa, D. Diaz-Diestra, D. Badillo-Diaz, R. Sharma, K. Dasari, S. Kumari, M. Holcomb, J. Beltran-Huarac, B. Weiner, and G. Morell, Controlling the transverse proton relaxivity of magnetic graphene oxide. *Scientific Reports*, **9**:5633, 2019.

[33] Y. Cao, Y. He, Z. Mao, Y. Kuang, M. Liu, Y. Zhang, and R. Pei, Synergistic regulation of longitudinal and transverse relaxivity of extremely small iron oxide nanoparticles (ESIONPs) using pH-responsive nanoassemblies. *Nanoscale*, **12**:17502, 2020.

[34] Hsu, B. Y. W., Wang, M., Zhang, Y., Vijayaragavan, V., Wong, S. Y., Chang, A. Y-C., Bhakoo, K. K., Li, X. and Wang, J. Silica–F127 nanohybrid-encapsulated manganese oxide nanoparticles for optimized T_1 magnetic resonance relaxivity, *Nanoscale,* 6:293, 2014.

[35] Yon, M., Gibot, L., Gineste, S., Laborie, P., Bijani, C., Mingotaud, C., Coutelier, O., Desmoulin, F., Pestourie, C., Destarac, M., Ciuculescu-Pradines, D. and Marty, J.-D. Assemblies of poly(N-vinyl-2-pyrrolidone)-based double hydrophilic block copolymers triggered by lanthanide ions: characterization and evaluation of their properties as MRI contrast agents. *Nanoscale*, 2023, **15**, 3893-3906.

[36] Song, Y., Zhu, Y., Jiang, K., Liu, X., Dong, L., Li, D., Chen, S., Xing, H., Yan, X., Lu, Y., Yang, X., Wang, J. and Xu, Y. Self-assembling ferrimagnetic fluorescent micelles for bioimaging guided efficient magnetic hyperthermia therapy. *Nanoscale*, 15:365, 2023.

[37] Du, H., Wang, Q., Liang, Z., Li, Q., Li, F. and Ling, D. Fabrication of magnetic nanoprobes for ultrahigh-field magnetic resonance imaging. *Nanoscale*, 14**:**17483, 2022.

[38] Duong, H. T. K., Abdibastami, A., Gloag, L., Barrera, L., Gooding, J. J. and Tilley, R. D. A guide to the design of magnetic particle imaging tracers for biomedical applications. *Nanoscale*, 14:13890, 2022.

[39] Nieves, L. M., Mossburg, K., Hsu, J. C., Maidment, A. D. A. and Cormode, D. P. Silver chalcogenide nanoparticles: a review of their biomedical applications. *Nanoscale,* 13:19306, 2021.

[40] Jiang, Q., Liu, X., Liang, G. and Sun, X. Self-assembly of peptide nanofibers for imaging applications. *Nanoscale*, 13:15142, 2021.

[41] Cao, Y., He, Y., Mao, Z., Kuang, Y., Liu, M., Zhang, Y. and Pei, R. Synergistic regulation of longitudinal and transverse relaxivity of extremely small iron oxide nanoparticles (ESIONPs) using pH-responsive nanoassemblies. *Nanoscale*, 12:17502, 2020.

[42] Sharma, V. K., Alipour, A., Soran-Erdem, Z., Aykut, Z. G. and Demir, H. V. Highly monodisperse low-magnetization magnetite nanocubes as simultaneous T_1–T_2 MRI contrast agents. *Nanoscale*, **7**:10519, 2015.